Solution-Processed Cd-Substituted CZTS Nanocrystals for Sensitized Liquid Junction Solar Cells

Sachin R. Rondiya[§*], Yogesh A. Jadhav[†*], Aleksandar Živković[¶], Sagar B. Jathar[†], Ganesh K. Rahane[†], Russell W. Cross[§], Avinash V. Rokade[†], Rupesh S. Devan[†], Sadhu Kolekar[†], Robert L. Z. Hoye[#], Hirendra N. Ghosh[‖], Nora H. de Leeuw[¶¥], Sandesh R. Jadkar[†*], Nelson Y. Dzade[§*]

[§]School of Chemistry, Cardiff University, Main Building, Park Place, Cardiff, CF10 3AT, Wales, United Kingdom

[†]School of Energy Studies, Savitribai Phule Pune University, Pune 411007, India

[¶]Department of Earth Sciences, Utrecht University, Princetonlaan 8a, 3548CB Utrecht, The Netherlands

[¥]School of Chemistry, University of Leeds, Woodhouse Lane, Leeds LS2 9JT, United Kingdom

[†]Department of Metallurgy Engineering & Materials Science, Indian Institute of Technology Indore, Simrol, Indore 453552, India

[#]Department of Materials, Imperial College London, Exhibition Road, London SW7 2AZ, UK

[‖]Institute of Nano Science and Technology, Mohali, Punjab 160062, India

Abstract

The Earth-abundant kesterite Cu_2ZnSnS_4 (CZTS) exhibits outstanding structural, optical, and electronic properties for a wide range of optoelectronic applications. However, the efficiency of CZTS thin-film solar cells is limited due to range of factors, including electronic disorder, secondary phases, and the presence of anti-site defects, which is key factor limiting the V_{oc}. The complete substitution of Zn lattice sites in CZTS nanocrystals (NCs) with Cd atoms offers a promising approach to overcome several of these intrinsic limitations. Herein, we investigate the effects of substitution of Cd^{2+} into Zn^{2+} lattice sites in CZTS NCs through a facile solution-based method. The structural, morphological, optoelectronic, and power conversion efficiencies (PCEs) of the NCs synthesized have been systematically characterized using various experimental techniques, and the results are corroborated by first-principles density functional theory (DFT) calculations. The successful substitution of Zn by Cd is demonstrated to induce a structural transformation from the kesterite phase to the stannite phase, which results in the bandgap reducing from 1.51 eV (kesterite) to 1.1 eV (stannite), which is closer to the optimum bandgap value for outdoor photovoltaic applications. Furthermore, the PCE of the novel Cd-substituted liquid junction solar cell underwent a four-fold increase, reaching 1.1%. These results highlight the importance of substitutional doping strategies in optimizing existing CZTS-based materials to achieve improved device characteristics.

Keywords: Cu_2CdSnS_4, solution-processed, phase transformation, cadmium substitution, liquid junction, first-principles density functional theory, photovoltaic.

Table of Content (TOC)

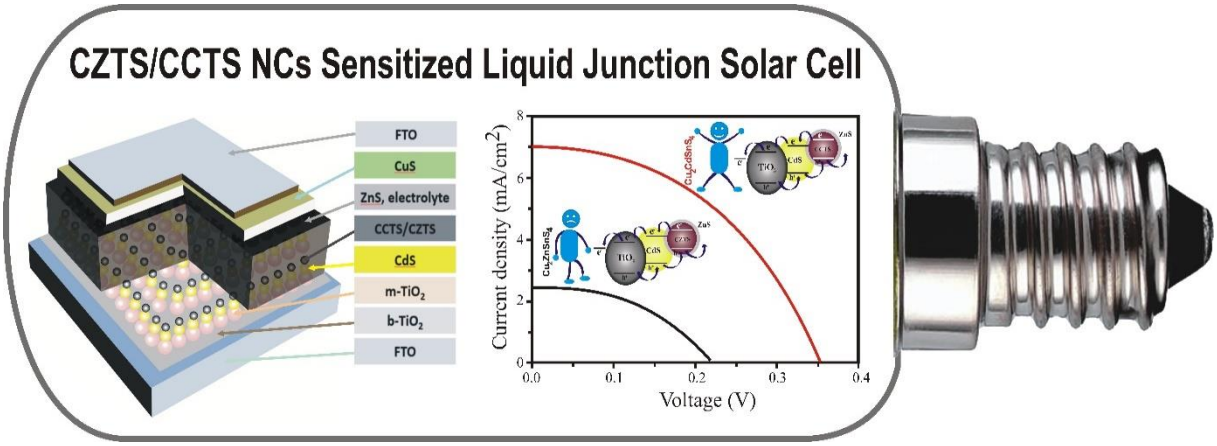

1. Introduction

Solar energy technologies are considered to be one of the most promising alternatives to fossil fuels to meet the rising demand of clean and renewable energy.[1–3] The sun provides such an amount of power to the Earth each second, that if harnessed after only a couple of hours could satisfy the entire human energy demand. However, significant improvements in the rational design of Earth-abundant absorber materials are still necessary before solar energy technology becomes more widely available.[4–6] Several research activities over the last decades have shown that the choice of suitable absorber materials coupled with efficient charge transport layers at the electrode-electrolyte interface are extremely important to achieve improved power conversion efficiencies.[7–9] As such, liquid junction solar cells (LJSCs) have received increased attention for next-generation photovoltaics.[10] In particular, LJSCs are more favourable than conventional dye-sensitized solar cells (DSSC) owing to their low fabrication cost.[11,12]

In general, LJSCs are composed of a semiconductor electrode and a counter electrode immersed in a suitable oxidation–reduction electrolyte.[13] In the past decade, binary semiconductor quantum dot materials, such as CdS, CdSe, CdTe, PbS or PbSe, have been employed as a sensitizer for quantum dot dye-sensitized solar cells (QDSSC).[14] However, most QDSSCs show a low power conversion efficiency (PCE) of up to 8%, due to their restricted light harvesting range.[15] Hence, to broaden the light absorption range, the binary sensitizer has been replaced by quaternary chalcopyrites, such as CIGSe or ZCISe, which have achieved PCEs of 11.49% and 12.57% as liquid junction QDSSCs, respectively.[16,17] There are some limitations to the commercialization of CIGSe and ZCISe solar cells, such as compositional uniformity, process control, toxicity, and difficulties in large-scale industrial manufacturing.[18]

Cu_2ZnSnS_4 (CZTS) has emerged as a promising alternative absorber candidate due to its composition of environmentally friendly and Earth-abundant elements, good absorption

coefficient (10^4 cm^{-1}), and direct optical band gap (1.0-1.5 eV).[19] Owing to these outstanding properties, Bai et al. achieved a PCE of 3.29% for CZTS QDSSCs by the hydrolysis approach and a PCE of 4.70% for CZTS/CdSe QDSSCs.[20] Further to this, Xu et al. used CZTS microsphere-coated FTO as a counter electrode and achieved a power conversion efficiency of 3.73%.[21] However, it has been reported that the PCE of CZTS sensitized solar cells are still lower than other types of sensitizers, due to insufficient light absorption, the presence of secondary phases, and short minority-carrier lifetimes.[11] Moreover, another major factor limiting the performance of kesterite CZTS is the formation of antisites (Cu_{zn}), which occurs due to the similar sizes of Cu and Zn ions.[22]

A recent study has shown that cation substitution by heavier atoms like Cd may inhibit the formation of antisite defects, thereby increasing the minority carrier lifetime and reducing electronic disorder in the system.[22] There are multiple benefits of Cd-substitution in CZTS. Due to a relatively large negative enthalpy of formation of ZnS, a narrow single-phase region and accompanying undesired secondary phases are formed in CZTS structures.[23] Cadmium sulfide (CdS), with a less negative enthalpy, can reduce secondary phases, therefore favouring the single-phase region of CCTS.[23] Recently, Rondiya et al. have employed a combined experimental and theoretical approach to determine the band alignment and offset at CCTS/CdS and CZTS/CdS hetero-interfaces, observing a smaller conduction band offset at the CCTS/CdS interface.[24] It has been reported that the effective minority carrier lifetimes of CZCTS and CZTS were calculated to be 10.8 and 4.1 ns, respectively, indicating that Cd incorporation improves the lifetime of the CZCTS absorber, which is crucial to achieve enhanced photocurrent.[25] Further, Yan et al. elaborated in detail how Cd alloying can improve the current density of CZTS.[26] This review indicates that the introduction of Cd exerts a beneficial impact on the efficiency of CZTS solar cells. However, to the best of our knowledge, there is no report available on the solution-processed Cd-substituted CZTS absorbers for nanocrystalline sensitized liquid junction solar cells.

In the present work, we have synthesized CCTS and CZTS nanocrystals through a cost-effective, low-temperature, and robust hot injection method. The crystal structure, size distribution, and surface morphology of the nanocrystals are characterized using X-ray diffraction (XRD), Raman spectrometry, (high-resolution) transmission electron microscopy (HR-TEM), X-ray photoelectron spectroscopy (XPS), and complementary density functional theory (DFT) calculations. The CZTS and CCTS devices were prepared by sandwiching the photo-anode (FTO/TiO_2/CdS/CZTS(CCTS)/ZnS) and counter electrode (CuS/FTO) using 50 μL electrolyte solution (S^{--}/S_n^{-}). We have used ZnS in a passivating layer to overcome charge carrier recombination. As a result, we observed an improvement in the current density (J_{sc}) and open circuit voltage (V_{oc}) parameters of the CCTS NCs sensitized solar cell compared to the CZTS counterpart. We have achieved 1.1% efficiency for CCTS NCs sensitized solar cell compared to 0.25% for CZTS, and to the best of our knowledge, this is the first report of PCE > 1% for CCTS NCs sensitized solar cells. We also anticipate that the efficiency of the CCTS NCs can be increased further through optimization of each layer in the device architecture.

2. Experimental and computational details

2.1 Chemicals: copper (II) acetylacetonate ($Cu(C_5H_7O_2)_2$, ≥ 97%), zinc acetylacetonate ($Zn(C_5H_7O_2)_2 \cdot xH_2O$, ≥ 99.99%), tin (IV) bis (acetylacetonate) dibromide ($[CH_3COCH=C(O-)CH_3]_2SnBr_2$, ≥ 97%), oleylamine (OAm, ≥ 99 %), isopropanol (IPA, ≥ 99.5%), toluene (≥ 99.8%), all were purchased from Sigma-Aldrich and used as-received.

***2.1 Synthesis*:** The colloidal synthesis of CZTS and CCTS nanocrystals (NCs) was carried out using the hot injection method as per our previous reports.[24,27,28]. In a typical synthesis of the CZTS NCs, copper (II) acetylacetonate (1.5 mmol), zinc acetylacetonate (0.75 mmol) and tin (IV) bis (acetylacetonate) dibromide (0.75 mmol) were dissolved in 15 mL oleylamine in a 100 mL three necked flask under inert atmosphere. The solution was initially heated to ~135 °C under vacuum and degassed for 1 hour and then maintained in nitrogen (N_2) until completion. This procedure was followed by an increase in temperature to 240 °C, which leads to the

formation of a metal oleylamine complex yielding a clear brown transparent solution. A freshly prepared sulfur precursor solution, 1 M sulfur powder dissolved in 3 mL oleylamine, was swiftly injected into the metal oleylamine complex colloidal solution which changed the solution color from transparent brown to a dark black. The flask temperature was maintained at 260 °C for 60 minutes to allow the growth of NCs. The temperature of the flask was then quickly brought down to ~ 80 °C by ice bath cooling. The reaction was further quenched by adding a solution of 5 mL of toluene and 40 mL of isopropanol. The colloidal solution from the flask was centrifuged at 10,000 rpm for 5 minutes, then the supernatant was decanted and the precipitate obtained. The process was repeated for the whole solution from the flask. The final precipitate obtained was then dispersed in isopropanol and the solution was transferred to a petri dish for drying. The final solid product was dried under vacuum and stored in a vacuum desiccator. The synthesis of CCTS NCs was carried out by a similar method, but zinc acetylacetonate was replaced with cadmium acetylacetonate. The schematic of the facile hot injection setup and synthesis steps for the synthesis of CZTS and CCTS NCs is shown in Scheme 1.

***2.2 Solar device fabrication*:** The fluorine-doped tin oxide (FTO) glass substrate was cleaned by isopropanol and distilled water followed by drying in an oven at 60 °C. The blocking layer was coated using $TiCl_4$ at 70 °C for 30 minutes. The first compact layer of TiO_2 (20 nm) and the second scattering layer of TiO_2 (~ 250 nm) were coated onto the FTO substrate using the doctor blade method.[29] After each layer of coating, the films were annealed at 450 °C for 1 hour. Over the FTO/TiO_2 layer, we have deposited CdS as the buffer layer using the SILAR method.[30] The light absorber materials CZTS and CCTS were then deposited by our unique room temperature method. The FTO/TiO_2/CdS electrodes were subjected to polarization for 10 min at 50 V in CZTS or CCTS NCs solution, which led to the formation of black colored CCTS and CZTS NCs films on the FTO/TiO_2/CdS electrode. Next, the sulfide/polysulfide electrolyte was prepared by dissolving 0.0329 gm/0.2 M sulfur, 0.237 g/0.6 M sodium sulfide, and 0.075

g/0.2 M KCl powders in 5 mL deionized water. The copper sulfide (CuS) counter electrode was prepared by an earlier reported process.[31] Metal contacts were made using indium wire, which were soldered on the FTO surface and employed as working and counter electrodes for the collection of charges. Finally, the FTO/TiO_2/CdS/CZTS/ZnS/S^{--}/S_n^-/CuS/FTO and FTO/TiO_2/CdS/CCTS/ZnS/S^{--}/S_n^-/CuS/FTO device architectures were prepared by sandwiching the photo-anode (FTO/TiO_2/CdS/CZTS/ZnS) and counter electrode (CuS/FTO) using 50 µL electrolyte (S^{--}/S_n^-). A spacer is also used to avoid a short circuit between the photo-anode and counter electrode. The solar cells were then sealed using binder clips prior to efficiency measurements.

***2.3 Characterization*:** The CZTS and CCTS NCs were characterized by several experimental techniques. X-ray diffraction (XRD) spectra were recorded by an X-ray diffractometer (Bruker D8 Advance, Germany). Raman spectroscopy data were obtained by He-Ne laser at 532 nm wavelength with the resolution of 1 cm^{-1}. During measurements, the power of the Raman laser was kept at less than 5 mW. High resolution transmission electron microscopy (HR-TEM) (TECNAI G2-20-TWIN) was used to obtain high resolution micrographs and selected area electron diffraction (SAED) patterns. X-ray photoelectron spectroscopy (XPS) was performed on the CZTS and CCTS samples with a Kratos Axis Ultra DLD photoelectron spectrometer, utilizing monochromatic AlKα radiation operating at an energy of 120 W. XPS data was analyzed using CasaXPS processing software. All XPS spectra were calibrated to the C (1s) line, taken to be 284.8 eV. The optical band gap was determined from absorbance spectra, measured using a JASCO, V-670 UV-Visible spectrophotometer in the range of 300-1600 nm. The photovoltaic characteristics of the CCTS and CZTS films were studied using a solar simulator system using an AM1.5 G spectrum with an illumination density of 100 W/m^2 at 25 °C.

***2.4 Computational details*:** Spin-polarized density functional theory (DFT) calculations were performed using the Vienna ab-initio simulation package (VASP) [32–34] with the projector-

augmented wave (PAW) method and a plane-wave cut-off of 350 eV. For the PAW potentials the valence electronic configurations used were $5s^2 4d^{10}$ for Cd, $4s^2 3d^{10}$ for Zn, $4s^1 3d^{10}$ for Cu, $5s^2 5p^2$ for Sn, and $3s^2 3p^4$ for S. The general gradient approximation (GGA) for the exchange-correlation (XC) functional was employed within the Perdew-Burke-Ernzerhof parametrization revised for solids (PBEsol).[35] Long-range dispersion corrections were included using the D3 approach of Grimme et al.[36] The conjugate gradient method was used for structural optimisations, with the total energy and force convergence criteria set to 10^{-5} eV and 0.01 eV/ Å. The Brillouin zone was sampled with a 5 x 5 x 3 Γ-centred Monkhorst-Pack mesh.[37] Suitable band paths compatible with crystal space group symmetry were identified using SeeK-path.[38,39] The distinct initial crystal structure for Kesterite CZTS and Stannite CCTS were taken from Hall *et al.* experimental measurements.[40] Lattice dynamics calculations were carried out within the harmonic approximation, using the PHONOPY package [41–43] to construct and evaluate the dynamical matrix. The finite displacement method (or the supercell approach) was used to construct the force constants. Vibrational frequency calculations presented were performed using the all-electron code CRYSTAL (2017 release) [44,45] with the hybrid B3LYP exchange-correlation functional.[46,47] The fraction of exact change (α) used in the hybrid functional was determined self-consistently (as the inverse of the dielectric constant) using the method by Skone *et al.*[48], with the dielectric constants determined using the coupled-perturbed Kohn-Sham method.[49] This self-consistent hybrid functional approach (SC-B3LYP) gave exact exchange percentages of 14.9949% (α=0.1499) for CZTS and 13.6063% (α=0.1361) for CCTS. The computed (averaged) dielectric constant ε is 6.675 for CZTS and 7.355 for CCTS. Various combinations of Gaussian-type basis sets available from the CRYSTAL library (https://www.crystal.unito.it/basis-sets.php) were tested in order to reproduce the geometry and electronic properties of CZTS and CCTS accurately. Long distance dispersion corrections were invoked using the D3 approach recently implemented in CRYSTAL.[36,50,51] The optimal basis sets taken (unmodified) were: all-electron Peintinger-

Oliveira-Bredow triple-ζ-valence + polarization (pob-TVZP) for Cd by Laun *et al.*[52], TZVP for Zn from Karttunen *et al.*[53], TZVP for Cu from Linnera *et al.*[54,55], effective core pseudopotential (SC-ECP) for Sn derived by Metz *et al.*[56], and 8-6311G* for S by Bredow *et al.*[57] In CRYSTAL, the convergence of the real-space summation of the Coulomb and exchange contributions to the Hamiltonian matrix is controlled by five overlap criteria. The values used in this study were 10^{-7}, 10^{-7}, 10^{-7}, 10^{-9}, and 10^{-30}. For the compounds of interest, the convergence with respect to k-points was checked. A Monkhorst-Pack mesh of 7 x 7 x 7 was used to sample the first Brillouin zone for both materials.[44] Relative Infra-red and Raman intensities were computed analytically, based on coupled-perturbed Hartree-Fock/Kohn-Sham (CPHF/KS) treatments implemented in the code.[58–60]

3. Result and Discussion

3.1 Structural properties of CZTS and CCTS nanocrystals (NCs): X-ray diffraction (XRD) measurements of CZTS-CCTS NCs were carried out to investigate the crystal phase. **Fig. 1(a)** shows the XRD pattern of the CZTS and CCTS NCs. The CZTS NCs are present in the kesterite phase (JCPDS No. 26-0575, space group $I\bar{4}$, number 82), which shows diffraction peaks at 28.48º, 32.98º, 47.38º, 56.2º, 58.78º, 69.13º, corresponding to the (112), (200), (220), (312), (224), and (332) planar orientations, respectively.[28] The CCTS NCs are present in the stannite (cernyite) phase (JCPDS No. 26-0506) and show diffraction peaks at 27.94º, 32.2º, 46.66º, 54.7º, which correspond to the (112), (200), (204), and (312) planes, respectively.[24] As was observed in previous reports, the shift of the (112) plane in XRD peak from $2\theta = 28.48^{o}$ for CZTS NCs to $2\theta = 27.94^{o}$ for CCTS NCs, confirms the replacement of Zn^{2+} with Cd^{2+}.[23] The average crystallite size, interplanar distance, strain, dislocation density, and lattice parameters of the CZTS and CCTS NCs are calculated from XRD spectra and reported in **Table 1**. Raman spectroscopy was carried out to confirm the phase purity of the as-synthesized CZTS and CCTS NCs as shown in **Fig. 1(b)**. The major peak at 336 cm^{-1} and shoulder peaks at 287.90 cm^{-1} correspond to the B_1 and A_1 mode of CZTS, which are consistent with previous literature

reports.[24] For the CCTS NCs, the main Raman peak at 325 cm^{-1} corresponds to the symmetric vibrational motion of a sulphur atom in the CCTS crystal structure, which confirms that no impurity phases are present in the CCTS NCs. The observed shift in the Raman spectra of CZTS (336 cm^{-1}) and CCTS (325 cm^{-1}) NCs is due to the exchange of Cd with Zn, which confirms a structural transition from I4 kesterite to I42m stannite, as was observed in the XRD patterns.[23,24] The low-resolution TEM images **Fig. 1(c and e)** show that the CZTS and CCTS NCs exhibit spherical shapes with diameters ranging from 15 to 35 nm. The high-resolution TEM (HR-TEM) pattern in **Fig. 1(d and f)** indicates that the NCs have lattice fringes with interplanar distances (*d*) of 0.311 nm and 0.319 nm, which match the (112) crystal planes of CZTS and CCTS NCs, respectively. It is clearly noticeable from the low resolution TEM images that CZTS and CCTS NCs have different orientations, which are marked by yellow circles in **Fig. 1(c and e)**. This further confirms that both CZTS and CCTS NCs are polycrystalline in nature.

3.2 Density functional theory (DFT): CZTS and CCTS crystallize in a tetragonal crystal structure in kesterite and stannite phases, respectively. The unit cell contains two formula units in which each atom is found in a tetrahedral environment. The calculated lattice parameters are listed in **Table 2**. Overall, both utilized approximations for the exchange-correlation functional yield results that are in satisfactory agreement with experimental values (lattice parameters, a (Å) and c (Å)), with the self-consistent hybrid functional showing smaller discrepancies. The tetragonal (kesterite) cell of CZTS (space group $I\bar{4}$, number 82) contains 16 atoms; its 48 vibrational modes can be further classified according to the irreducible representation of the $\bar{4}$ point group as follows:

$$\Gamma_{total} = 3A \oplus 7B \oplus 7^1E \oplus 7^2E.$$

A, B, and E (doubly degenerate) are Raman active modes, while B and E (doubly degenerate) are IR active. The tetragonal (stannite) cell of CCTS (space group $I\bar{4}$2m, number 121) contains

a total of 16 atoms, giving rise to 48 vibrational modes which further can be classified according to the irreducible representations of the $\bar{4}$2m point group as follows:

$$\Gamma_{total} = 2A_1 \oplus 1A_2 \oplus 2B_1 \oplus 5B_2 \oplus 7E.$$

A_1, A_2, B_1, and E (doubly degenerate) are Raman active, B_2 and E (doubly degenerate) are IR active, and A_2 is silent.

Computed values of the Raman active modes in CZTS and CCTS are reported in **Table 3**, while the corresponding spectra are shown in **Fig. 2 (a and b),** respectively. Despite the slight overestimation observed for the Raman mode frequency, the overall spectra are reproduced satisfactorily for both compounds. Graphical animations identify the most prominent (asymmetric) peaks at 340.65 cm^{-1} and 301.70 cm^{-1} for CZTS, as well as 331.97 cm^{-1} for CCTS, to originate entirely from a combined stretch-bending S mode. The subsequent most eminent features in the spectra of CZTS, at 261.27 cm^{-1} and 270.25 cm^{-1} (double-degenerate), are attributed to in-plane vibrations and vibrations of all atoms in a disordered pattern, respectively. The eminent mode found at 253.10 cm^{-1} in CCTS (double degenerate, symmetry species *E*) is assigned to vibrations of all four atoms, with the strongest contribution coming from the S and Cu atoms. The calculated phonon dispersion across the first Brillouin zone together with the atom projected partial phonon densities of state (DOS) for CZTS and CCTS are shown in **Fig. 3 (a and b)**, respectively. No imaginary modes (negative frequencies or soft modes) were found throughout the first Brillouin zone, satisfying the crystal stability condition which states that the lattice needs to be stable with respect to any small atomic displacement.[61] This means that both compounds are stable at ambient pressure. Replacing Zn with Cd, however, does introduce more phonon states at lower frequencies (pDOS graph), around 1.75 THz. However, those do not induce strong acoustic mode softening to drive a dynamic instability of CCTS.

3.3 Oxidation state and compositional analyses of CZTS and CCTS nanocrystals (NCs): The electronic and chemical properties of CZTS and CCTS materials are confirmed from XPS. **Fig. 4** shows the XPS spectrum for the as-synthesized CZTS (left panel) and CCTS (right panel)

NCs, respectively. All the spectra are deconvoluted via a Voigt curve fitting function in the Shirley background. The high-resolution XPS spectrum in **Fig. 4(a)** shows 4 well-defined peaks of Cu($2p_{3/2}$), shake-up satellite of Cu($2p_{3/2}$), Cu($2p_{1/2}$), and shake-up satellite of Cu($2p_{1/2}$), sequentially. Furthermore, deconvolution of Cu(2p) shows a perfect fit for 8 peaks of Cu^{2+}($2p_{3/2}$), Cu^{3+}($2p_{3/2}$), shake up satellite of Cu^{2+}($2p_{3/2}$), shake up satellite of Cu^{3+}($2p_{3/2}$), Cu^{2+}($2p_{1/2}$), Cu^{3+}($2p_{1/2}$), shake up satellite of Cu^{2+}($2p_{1/2}$), and shake up satellite of Cu^{3+}($2p_{1/2}$) located at binding energies of 933.22(≡a), 936.39 (≡a′), 941.15 (≡b), 944.87 (≡b′), 953.07 (≡c), 956.37 (≡c′), 961.05 (≡d), and 964.11 (≡d′), respectively. The double peak features of Cu(2p) and their accompanying shake-up satellite peaks illustrate the existence of Cu^{2+} ions and an open $3d^9$ shell of Cu^{2+}.[62,63] The energy separation of 19.85 (± 0.05) eV observed between Cu^{2+}($2p_{3/2}$) and Cu^{2+}($2p_{1/2}$), and their shake-up satellite peaks, is assigned to the formation of Cu^{2+}, and not of Co^0 or Cu^{1+}.[63] The deconvolution of the XPS spectrum of Cu(2p) in **Fig. 4(e)** illustrates the presence of Cu^{2+} ions in the CCTS NCs, owing to their similarity with the peak positions of CZTS NCs in **Fig. 4(a)**. Furthermore, the Zn(2p) XPS spectrum (**Fig. 4(b)**) shows the double peak features of Zn($2p_{3/2}$) and Zn($2p_{1/2}$) located at binding energies of 1023.28 and 1046.18 eV, respectively, with an energy separation of 22.9 eV, which reveals the appearance of Zn^{2+} ions in the CZTS NCs. The Zn($2p_{3/2}$) peak position is relatively higher than the values reported for ZnS (*i.e.*, 1021.2 eV),[64] ZnO (*i.e.*, 1020.8-1022.58 eV),[65] and pure metallic Zn (*i.e.*, 1021.00- 1021.58 eV) [65,66], indicating that Zn forms ZnS as the intermediate phase. The double peak feature of Cd(3d) in **Fig. 4(f)** is deconvoluted into two peaks of Cd($3d_{5/2}$) and Cd($3d_{3/2}$) located at binding energies of 405.76 and 412.51 eV, respectively, with an energy separation of 6.75 eV, which confirms the existence of Cd^{2+} ions in the CCTS NCs. The Cd($3d_{5/2}$) peak position is observed at a ~1-2 eV higher binding energy than that reported for CdS thin films and nanoparticles (*i.e.*, 403.75-404.88 eV).[67–69] This shift in binding energy in CCTS is akin to our observation in the CZTS NCs and may be ascribed to the existence of Cd in the surrounding of Cu and Sn. The deconvolution of Sn(3d)

shows the perfect fit for two peaks of Sn($3d_{5/2}$) and Sn($3d_{3/2}$) located at binding energies of 487.37 (± 0.10) (≡ a) eV and 495.78 (±0.12) (≡ b) eV, respectively, which in both CZTS, **Fig. 4(c)**, and CCTS, **Fig. 4(g)**, NCs, are assigned to Sn^{4+} ions. The Sn($3d_{5/2}$) peak position observed at a ~2.4 eV higher binding energy than that of Sn^0 (*i.e.*, 485.0 eV) ruled out the existence of unreacted Sn in CZTS NCs. However, the shoulder peaks at binding energies of 485.72 (≡a′) and 494.13 eV (≡b′) are observed for CCTS NCs. The intensity of these peaks is relatively inferior to those assigned to Sn^{4+}($3d_{5/2}$) and Sn^{4+}($3d_{3/2}$), indicating only negligible existence of metallic Sn^0.[70] An energy separation of ≥ 8.4 eV is observed for both the samples. Likewise, the deconvolution of the XPS spectra for S(2p) shows the reasonable fit for three peaks located at binding energies of 162.47 (±0.33), 163.78 (±0.33) and 169.40 (±0.18) eV for CZTS (**Fig. 4(d)**) and CCTS (**Fig. 4(h)**) NCs. The peaks S($2p_{3/2}$) and S($2p_{1/2}$) assigned to the binding energies of 162.47 (±0.33), and 163.78 (±0.33) confirm the formation of a S^{2-} anion.[69,71] The energy separation of 1.80 (± 0.02) eV observed between S($2p_{3/2}$) and S($2p_{1/2}$) is akin to the values reported in the literature and may be attributed to the existence of completely sulfurized CZT and CCdT NCs.[70,71] The peak at a higher binding energy of 169.40 (±0.18) eV is assigned to SO_4^{2-}, indicating the existence of sulfate species at the surface of both CZTS and CCTS NCs. Overall, the XPS analyses confirm the formation of pure-phase CZTS and CCTS NCs without the growth of undesired phases, or oxidized phases. Most importantly, the replacement of Zn by Cd does not significantly alter the chemical and electronic properties of the Cu, Sn, and S elements in the CCTS NCs.

3.4 Optical properties of CZTS and CCTS nanocrystals (NCs): The experimental room-temperature absorbance UV-Vis-NIR spectra of CZTS and CCTS are shown in **Fig. 5(a)**. The spectra reveal photo-absorption in the entire visible region with a tail extending to the near-IR (NIR) region. The Tauc plot for both NCs (insert in **Fig. 5(a)**), was used to estimate the band gap based on the allowed direct inter-band transitions. The optical band gap of CZTS and CCTS were found to be 1.51 eV and 1.10 eV, respectively. The band gap of CCTS is close to the

optimum bandgap for single-junction devices under 1-sun radiation, indicating that CCTS material holds promise for photovoltaic applications.

3.5 Nanocrystals sensitized liquid junction solar cell: Shown in **Fig. 5(c)** is the schematic diagram of the photovoltaic device fabricated with CZTS and CCTS NCs in the FTO/TiO_2/CdS/CZ(Cd)TS/ZnS/S^{--}/S_n^{-}/CuS/FTO architecture with 0.25 cm^2 active area. To investigate the photovoltaic properties of the CZTS and CCTS NCs sensitized solar cells, we measured their J-V curves under AM 1.5G illumination. The measured open-circuit voltage (Voc), current density (Jsc), fill factor (FF) and efficiency (η) for CZTS NCs sensitized solar cells are found to be 0.22 V, 2.48 mA/cm^{-2}, 0.44, and 0.25%, respectively (**Fig. 5(b**) and **Table 4**), whereas for the CCTS NCs sensitized solar cell, the Voc, Jsc, FF, and η values are found to be 0.35 V, 7.03 mA/cm^{-2}, 0.44, and 1.1%, respectively (**Fig. 5(b**) and **Table 4**). The significant improvement in the Voc and Jsc parameters of the CCTS NCs sensitized solar cell can be attributed to its increased light harvesting ability and improved electron transport. The proposed schematic diagram shows the flow of photo-generated electrons and holes in the device as depicted by the arrows in **Fig. 5(**d**)**. Further improvements in performance could be achieved by increasing grain size, improving structural order to obtain a sharper absorption edge, and reducing the density of defects in the film. It has been reported that sulfurization has led to an increase in grain size and more stoichiometric and structural order.[72–74] The use of annealed CZTS films as the light absorbing layer have shown improvied efficiencies compared to the non-annealed films.[75–78] There are variety of reported chemical treatments which have been shown to improve the efficiency.[79–81] Although in the present investigation the obtained device efficiency is low, it is important to note that the absorber layers were not further processed after deposition with any high-temperature or chemical treatments. Hence, further optimization of the synthesis and device fabrication could lead to even better device characteristics. Bai et.al reported 0.19% efficiency using the hydrolysis approach.[20], and also with hydrolysis, CZTS QDSSCs achieved an impressive conversion efficiency of 3.29% with a

high short-circuit current of 17.48 mA cm^{-2}.[20] Ji et.al. reported 1% efficiency for a CZTS based QDSSC solar cell with a route to phase controllable $Cu_2ZnSn(S_{1-x}Se_x)_4$ nanocrystals.[82] To the best of our knowledge, this study is the first report of the power conversion efficiency (PCE) > 1% for a CCTS NCs sensitized solar cell. Further work in optimization of device fabrication is expected to increase the efficiency of CCTS NCs sensitized solar cell. Specifically, for the FTO/TiO_2/CdS/CCTS/ZnS/S^{--}/S_n^-/CuS/FTO device architecture, optimization of each layer thickness and interface will reduce carrier trapping and should be addressed in future investigations.

4. Summary and Conclusion

We have successfully synthesised Cd-substituted CZTS NCs (CCTS) using the hot-injection method and highlighted the advantages of Cd incorporation in CZTS for nanocrystal sensitised liquid junction solar cell fabrication. Highly crystalline phase-pure CZTS and CCTS NCs were obtained in the kesterite and the stannite phases, respectively, and a bandgap reduction from 1.51 eV (CZTS) to 1.1 eV (CCTS) was demonstrated. Consistent with its optimum band gap, the fabricated CCTS NCs sensitized solar cell shows superior device characteristics (Voc = 0.35 V, Jsc = 7.03 mA/cm^{-2}, FF = 0.44, and η = 1.1%) than that of the equivalent CZTS device. This work should attract further investigations to obtain the controlled synthesis of solution-processed CCTS NCs with improved structural and optoelectronic properties, lower defect density, as well as optimized p–n junction device structures to achieve improved PV performance.

Acknowledgements

S.R.R., R.W.C., and N.Y.D. acknowledge the UK Engineering and Physical Sciences Research Council (EPSRC) for funding (Grant No. EP/S001395/1). A.Z. and N.H.d.L acknowledge the Netherlands Research Council NWO (ECHO grant 712.018.005). Y.A.J. thanks SPPU PDF and School of Energy Studies, SPPU for financial support and access to laboratory facilities. This work has also used the computational facilities of the Advanced Research Computing at Cardiff

(ARCCA) Division, Cardiff University, and HPC Wales. This work also made use of the facilities of ARCHER (http://www.archer.ac.uk), the UK's national supercomputing service via the membership of the UK's HEC Materials Chemistry Consortium, which is funded by EPSRC (EP/L000202).

References

[1] M.M. Lee, J. Teuscher, T. Miyasaka, T.N. Murakami, H.J. Snaith, Efficient hybrid solar cells based on meso-superstructured organometal halide perovskites, Science (80-.). 338 (2012) 643–647. https://doi.org/10.1126/science.1228604.

[2] V.S. Waman, M.M. Kamble, S.S. Ghosh, A.H. Mayabadi, B.B. Gabhale, S.R. Rondiya, A. V. Rokade, S.S. Khadtare, V.G. Sathe, H.M. Pathan, S.W. Gosavi, S.R. Jadkar, Evolution of microstructure and opto-electrical properties in boron doped nc-Si:H films deposited by HW-CVD method, J. Alloys Compd. 585 (2014) 523–528. https://doi.org/10.1016/j.jallcom.2013.09.172.

[3] A. Jadhavar, A. Pawbake, R. Waykar, V. Jadkar, R. Kulkarni, A. Bhorde, S. Rondiya, A. Funde, D. Patil, A. Date, H. Pathan, S. Jadkar, Growth of Hydrogenated Nano-crystalline Silicon (nc-Si:H) Films by Plasma Enhanced Chemical Vapor Deposition (PE-CVD), in: Energy Procedia, 2017: pp. 45–52. https://doi.org/10.1016/j.egypro.2017.03.104.

[4] K. Diwate, S. Rondia, A. Mayabadi, A. Rokade, R. Waykar, H. Borate, A. Funde, M. Shinde, M.B. Rajedra Prasad, H. Pathan, S. Jadkar, Chemical spray pyrolysis synthesis of covellite copper sulphide (CuS) thin films for economical counter electrode for DSSCs, J. Mater. Sci. Mater. Electron. 29 (2018) 4940–4947. https://doi.org/10.1007/s10854-017-8453-6.

[5] T.K. Todorov, J. Tang, S. Bag, O. Gunawan, T. Gokmen, Y. Zhu, D.B. Mitzi, Beyond 11% effi ciency: Characteristics of state-of-the-art Cu 2ZnSn(S,Se)4Solar Cells, Adv. Energy Mater. 3 (2013) 34–38. https://doi.org/10.1002/aenm.201200348.

[6] S. Rondiya, A. Rokade, B. Gabhale, S. Pandharkar, M. Chaudhari, A. Date, M. Chaudhary, H. Pathan, S. Jadkar, Effect of Bath Temperature on Optical and Morphology Properties of CdS Thin Films Grown by Chemical Bath Deposition, in: Energy Procedia, 2017: pp. 202–209. https://doi.org/10.1016/j.egypro.2017.03.128.

[7] A. Rokade, S. Rondiya, A. Date, V. Sharma, M. Prasad, H. Pathan, S. Jadkar, Electrochemical Synthesis of Core-shell ZnO/CdS Nanostructure for Photocatalytic

Water Splitting Application, in: Energy Procedia, 2017: pp. 121–127. https://doi.org/10.1016/j.egypro.2017.03.116.

[8] J. Chen, N.G. Park, Materials and Methods for Interface Engineering toward Stable and Efficient Perovskite Solar Cells, ACS Energy Lett. 5 (2020) 2742–2786. https://doi.org/10.1021/acsenergylett.0c01240.

[9] A.C. Society, M. Id, M. Type, A.D. Submitted, C. List, E.S. Rondiya, C. Jadhav, C. Nilegave, E.S. Cross, C. Barma, E.S. Nasane, E.S. Gaware, E.S. Bade, P. Jadkar, P. Funde, E.S. Dzade, Ternary Cu 2 SnS 3 : Synthesis , Structure , Photoelectrochemical Activity , and, Chem. Mater. (2020) acs.chemmater.0c03223. https://doi.org/10.1021/acs.chemmater.0c03223%0Ahttps://pubs.acs.org/doi/10.1021/acs.chemmater.0c03223.

[10] C.-L. Chou, N. Suriyawong, B. Aragaw, J.-B. Shi, M.-W. Lee, Ag 3 SbS 3 Liquid-Junction Semiconductor-Sensitized Solar Cells , J. Electrochem. Soc. 163 (2016) H445–H449. https://doi.org/10.1149/2.1121606jes.

[11] M. Aftab Akram, S. Javed, M. Islam, M. Mujahid, A. Safdar, Arrays of CZTS sensitized ZnO/ZnS and ZnO/ZnSe core/shell nanorods for liquid junction nanowire solar cells, Sol. Energy Mater. Sol. Cells. 146 (2016) 121–128. https://doi.org/10.1016/j.solmat.2015.11.034.

[12] P. V. Kamat, K. Tvrdy, D.R. Baker, J.G. Radich, Beyond photovoltaics: Semiconductor nanoarchitectures for liquid-junction solar cells, Chem. Rev. 110 (2010) 6664–6688. https://doi.org/10.1021/cr100243p.

[13] A. Kolay, D. Maity, P. Ghosal, M. Deepa, Carbon@Tellurium Nanostructures Anchored to a Si Nanowire Scaffold with an Unprecedented Liquid-Junction Solar Cell Performance, ACS Appl. Mater. Interfaces. 11 (2019) 47972–47983. https://doi.org/10.1021/acsami.9b17573.

[14] A. Manjceevan, J. Bandara, Systematic stacking of PbS/CdS/CdSe multi-layered quantum dots for the enhancement of solar cell efficiency by harvesting wide solar spectrum, Electrochim. Acta. 271 (2018) 567–575. https://doi.org/10.1016/j.electacta.2018.03.193.

[15] K. Zhao, Z. Pan, I. Mora-Seró, E. Cánovas, H. Wang, Y. Song, X. Gong, J. Wang, M. Bonn, J. Bisquert, X. Zhong, Boosting power conversion efficiencies of quantum-dot-sensitized solar cells beyond 8% by recombination control, J. Am. Chem. Soc. 137 (2015) 5602–5609. https://doi.org/10.1021/jacs.5b01946.

[16] W. Peng, J. Du, Z. Pan, N. Nakazawa, J. Sun, Z. Du, G. Shen, J. Yu, J.S. Hu, Q. Shen,

X. Zhong, Alloying Strategy in Cu-In-Ga-Se Quantum Dots for High Efficiency Quantum Dot Sensitized Solar Cells, ACS Appl. Mater. Interfaces. 9 (2017) 5328–5336. https://doi.org/10.1021/acsami.6b14649.

[17] L. Zhang, Z. Pan, W. Wang, J. Du, Z. Ren, Q. Shen, X. Zhong, Copper deficient Zn-Cu-In-Se quantum dot sensitized solar cells for high efficiency, J. Mater. Chem. A. 5 (2017) 21442–21451. https://doi.org/10.1039/c7ta06904a.

[18] J. Ramanujam, U.P. Singh, Copper indium gallium selenide based solar cells - A review, Energy Environ. Sci. 10 (2017) 1306–1319. https://doi.org/10.1039/c7ee00826k.

[19] S. Rondiya, A. Rokade, P. Sharma, M. Chaudhary, A. Funde, Y. Jadhav, S. Haram, H. Pathan, S. Jadkar, CZTS/CdS: interface properties and band alignment study towards photovoltaic applications, J. Mater. Sci. Mater. Electron. 29 (2018) 4201–4210. https://doi.org/10.1007/s10854-017-8365-5.

[20] B. Bai, D. Kou, W. Zhou, Z. Zhou, S. Wu, Application of quaternary Cu2ZnSnS4 quantum dot-sensitized solar cells based on the hydrolysis approach, Green Chem. 17 (2015) 4377–4382. https://doi.org/10.1039/c5gc01049g.

[21] J. Xu, X. Yang, Q.D. Yang, T.L. Wong, C.S. Lee, Cu 2ZnSnS 4 hierarchical microspheres as an effective counter electrode material for quantum dot sensitized solar cells, J. Phys. Chem. C. 116 (2012) 19718–19723. https://doi.org/10.1021/jp306628m.

[22] J. Fu, Q. Tian, Z. Zhou, D. Kou, Y. Meng, W. Zhou, S. Wu, Improving the Performance of Solution-Processed Cu2ZnSn(S,Se)4 Photovoltaic Materials by Cd2+ Substitution, Chem. Mater. 28 (2016) 5821–5828. https://doi.org/10.1021/acs.chemmater.6b02111.

[23] Z. Su, J.M.R. Tan, X. Li, X. Zeng, S.K. Batabyal, L.H. Wong, Cation Substitution of Solution-Processed Cu2ZnSnS4 Thin Film Solar Cell with over 9% Efficiency, Adv. Energy Mater. 5 (2015). https://doi.org/10.1002/aenm.201500682.

[24] S.R. Rondiya, Y. Jadhav, N.Y. Dzade, R. Ahammed, T. Goswami, A. De Sarkar, S. Jadkar, S. Haram, H.N. Ghosh, Experimental and Theoretical Study into Interface Structure and Band Alignment of the Cu2Zn1-xCdxSnS4Heterointerface for Photovoltaic Applications, ACS Appl. Energy Mater. 3 (2020) 5153–5162. https://doi.org/10.1021/acsaem.9b02314.

[25] C. Yan, K. Sun, J. Huang, S. Johnston, F. Liu, B.P. Veettil, K. Sun, A. Pu, F. Zhou, J.A. Stride, M.A. Green, X. Hao, Beyond 11% Efficient Sulfide Kesterite Cu2ZnxCd1-xSnS4 Solar Cell: Effects of Cadmium Alloying, ACS Energy Lett. 2 (2017) 930–936.

https://doi.org/10.1021/acsenergylett.7b00129.

[26] C. Yan, K. Sun, J. Huang, S. Johnston, F. Liu, B.P. Veettil, K. Sun, A. Pu, F. Zhou, J.A. Stride, M.A. Green, X. Hao, Beyond 11% Efficient Sulfide Kesterite Cu 2 Zn x Cd 1– x SnS 4 Solar Cell: Effects of Cadmium Alloying, ACS Energy Lett. 2 (2017) 930–936. https://doi.org/10.1021/acsenergylett.7b00129.

[27] Y.A. Jadhav, P.R. Thakur, S.K. Haram, Voltammetry investigation on copper zinc tin sulphide /selenide (CZTSxSe1-x) alloy nanocrystals: Estimation of composition dependent band edge parameters, Sol. Energy Mater. Sol. Cells. 155 (2016) 273–279. https://doi.org/10.1016/j.solmat.2016.06.030.

[28] S. Pandharkar, S. Rondiya, A. Bhorde, S. Nair, R. Aher, P. Vairale, A. Waghmare, D. Naik, R. Waykar, Y. Jadhav, S. Haram, M.K. Ghosalya, C. Gopinath, M. Prasad, S. Jadkar, Probing the effect of selenium substitution in kesterite-Cu2ZnSnS4 nanocrystals prepared by hot injection method, J. Mater. Sci. Mater. Electron. 30 (2019) 14781–14790. https://doi.org/10.1007/s10854-019-01851-7.

[29] N. Nang Dinh, N. Minh Quyen, D.N. Chung, M. Zikova, V. Van Truong, Highly-efficient electrochromic performance of nanostructured TiO 2 films made by doctor blade technique, Sol. Energy Mater. Sol. Cells. 95 (2011) 618–623. https://doi.org/10.1016/j.solmat.2010.09.028.

[30] B.R. Sankapal, R.S. Mane, C.D. Lokhande, Deposition of CdS thin films by the Successive Ionic Layer Adsorption and Reaction (SILAR) method, Mater. Res. Bull. 35 (2000) 177–184. https://doi.org/10.1016/S0025-5408(00)00210-5.

[31] J. Dana, P. Anand, S. Maiti, F. Azlan, Y. Jadhav, S.K. Haram, H.N. Ghosh, Inhibiting Interfacial Charge Recombination for Boosting Power Conversion Efficiency in CdSe{Au} Nanohybrid Sensitized Solar Cell, J. Phys. Chem. C. 122 (2018) 13277–13284. https://doi.org/10.1021/acs.jpcc.7b08448.

[32] D. Joubert, From ultrasoft pseudopotentials to the projector augmented-wave method, Phys. Rev. B - Condens. Matter Mater. Phys. 59 (1999) 1758–1775. https://doi.org/10.1103/PhysRevB.59.1758.

[33] G. Kresse, J. Furthmüller, Efficient iterative schemes for ab initio total-energy calculations using a plane-wave basis set, Phys. Rev. B - Condens. Matter Mater. Phys. 54 (1996) 11169–11186. https://doi.org/10.1103/PhysRevB.54.11169.

[34] G. Kresse, J. Furthmüller, Efficiency of ab-initio total energy calculations for metals and semiconductors using a plane-wave basis set, Comput. Mater. Sci. 6 (1996) 15–50. https://doi.org/10.1016/0927-0256(96)00008-0.

[35] G.I. Csonka, J.P. Perdew, A. Ruzsinszky, P.H.T. Philipsen, S. Lebègue, J. Paier, O.A. Vydrov, J.G. Ángyán, Assessing the performance of recent density functionals for bulk solids, Phys. Rev. B - Condens. Matter Mater. Phys. 79 (2009). https://doi.org/10.1103/PhysRevB.79.155107.

[36] S. Grimme, J. Antony, S. Ehrlich, H. Krieg, A consistent and accurate ab initio parametrization of density functional dispersion correction (DFT-D) for the 94 elements H-Pu, J. Chem. Phys. 132 (2010). https://doi.org/10.1063/1.3382344.

[37] H.J. Monkhorst, J.D. Pack, Special points for Brillouin-zone integrations, Phys. Rev. B. 13 (1976) 5188–5192. https://doi.org/10.1103/PhysRevB.13.5188.

[38] A. Togo, I. Tanaka, $\texttt{Spglib}$: a software library for crystal symmetry search, 2018. http://arxiv.org/abs/1808.01590.

[39] Y. Hinuma, G. Pizzi, Y. Kumagai, F. Oba, I. Tanaka, Band structure diagram paths based on crystallography, Comput. Mater. Sci. 128 (2017) 140–184. https://doi.org/10.1016/j.commatsci.2016.10.015.

[40] S.R. Hall, J.T. Szymanski, J.M. Stewart, Kesterite, Cu2(Zn,Fe)SnS4 and Stannite Cu2(Fe,Zn)SnS4, structurally similar but distinct minerals, Can. Mineral. 16 (1978) 131–137. http://canmin.geoscienceworld.org/cgi/content/abstract/16/2/131.

[41] A. Togo, I. Tanaka, First principles phonon calculations in materials science, Scr. Mater. 108 (2015) 1–5. https://doi.org/10.1016/j.scriptamat.2015.07.021.

[42] J.M. Skelton, S.C. Parker, A. Togo, I. Tanaka, A. Walsh, Thermal physics of the lead chalcogenides PbS, PbSe, and PbTe from first principles, Phys. Rev. B - Condens. Matter Mater. Phys. 89 (2014). https://doi.org/10.1103/PhysRevB.89.205203.

[43] A. Togo, L. Chaput, I. Tanaka, G. Hug, First-principles phonon calculations of thermal expansion in Ti 3SiC2, Ti3AlC2, and Ti 3GeC2, Phys. Rev. B - Condens. Matter Mater. Phys. 81 (2010). https://doi.org/10.1103/PhysRevB.81.174301.

[44] I. and others Dovesi, R and Saunders, VR and Roetti, C and Orlando, R and Zicovich-Wilson, CM and Pascale, F and Civalleri, B and Doll, K and Harrison, NM and Bush, CRYSTAL17 User's Manual, Gruppo di Chimica Teorica, Dipartimento di Chimica, 2017.

[45] R. Dovesi, A. Erba, R. Orlando, C.M. Zicovich-Wilson, B. Civalleri, L. Maschio, M. Rérat, S. Casassa, J. Baima, S. Salustro, B. Kirtman, Quantum-mechanical condensed matter simulations with CRYSTAL, Wiley Interdiscip. Rev. Comput. Mol. Sci. 8 (2018). https://doi.org/10.1002/wcms.1360.

[46] A.D. Becke, A new mixing of Hartree-Fock and local density-functional theories, J.

Chem. Phys. 98 (1993) 1372–1377. https://doi.org/10.1063/1.464304.

[47] C. Lee, W. Yang, R.G. Parr, Development of the Colle-Salvetti correlation-energy formula into a functional of the electron density, Phys. Rev. B. 37 (1988) 785–789. https://doi.org/10.1103/PhysRevB.37.785.

[48] J.H. Skone, M. Govoni, G. Galli, Self-consistent hybrid functional for condensed systems, Phys. Rev. B - Condens. Matter Mater. Phys. 89 (2014). https://doi.org/10.1103/PhysRevB.89.195112.

[49] M. Ferrero, M. Rérat, R. Orlando, R. Dovesi, I.J. Bush, Coupled perturbed Kohn-Sham calculation of static polarizabilities of periodic compounds, in: J. Phys. Conf. Ser., 2008. https://doi.org/10.1088/1742-6596/117/1/012016.

[50] S. Grimme, S. Ehrlich, L. Goerigk, Effect of the damping function in dispersion corrected density functional theory, J. Comput. Chem. 32 (2011) 1456–1465. https://doi.org/10.1002/jcc.21759.

[51] S. Grimme, A. Hansen, J.G. Brandenburg, C. Bannwarth, Dispersion-Corrected Mean-Field Electronic Structure Methods, Chem. Rev. 116 (2016) 5105–5154. https://doi.org/10.1021/acs.chemrev.5b00533.

[52] J. Laun, D. Vilela Oliveira, T. Bredow, Consistent gaussian basis sets of double- and triple-zeta valence with polarization quality of the fifth period for solid-state calculations, J. Comput. Chem. 39 (2018) 1285–1290. https://doi.org/10.1002/jcc.25195.

[53] A.J. Karttunen, T. Tynell, M. Karppinen, Atomic-level structural and electronic properties of hybrid inorganic-organic ZnO:Hydroquinone superlattices fabricated by ALD/MLD, J. Phys. Chem. C. 119 (2015) 13105–13114. https://doi.org/10.1021/acs.jpcc.5b03433.

[54] J. Linnera, A.J. Karttunen, Ab initio study of the lattice thermal conductivity of Cu2 O using the generalized gradient approximation and hybrid density functional methods, Phys. Rev. B. 96 (2017). https://doi.org/10.1103/PhysRevB.96.014304.

[55] J. Linnera, G. Sansone, L. Maschio, A.J. Karttunen, Thermoelectric Properties of p-Type Cu2O, CuO, and NiO from Hybrid Density Functional Theory, J. Phys. Chem. C. 122 (2018) 15180–15189. https://doi.org/10.1021/acs.jpcc.8b04281.

[56] B. Metz, H. Stoll, M. Dolg, Small-core multiconfiguration-Dirac-Hartree-Fock-adjusted pseudopotentials for post-d main group elements: Application to PbH and PbO, J. Chem. Phys. 113 (2000) 2563–2569. https://doi.org/10.1063/1.1305880.

[57] T. Bredow, P. Heitjans, M. Wilkening, Electric field gradient calculations for LixTiS2

and comparison with 7Li NMR results, Phys. Rev. B - Condens. Matter Mater. Phys. 70 (2004) 115111. https://doi.org/10.1103/PhysRevB.70.115111.

[58] L. Maschio, B. Kirtman, R. Orlando, M. Rèrat, Ab initio analytical infrared intensities for periodic systems through a coupled perturbed Hartree-Fock/Kohn-Sham method, J. Chem. Phys. 137 (2012). https://doi.org/10.1063/1.4767438.

[59] L. Maschio, B. Kirtman, M. Rérat, R. Orlando, R. Dovesi, Ab initio analytical Raman intensities for periodic systems through a coupled perturbed Hartree-Fock/Kohn-Sham method in an atomic orbital basis. II. Validation and comparison with experiments, J. Chem. Phys. 139 (2013). https://doi.org/10.1063/1.4824443.

[60] L. Maschio, B. Kirtman, M. Rérat, R. Orlando, R. Dovesi, Ab initio analytical Raman intensities for periodic systems through a coupled perturbed Hartree-Fock/Kohn-Sham method in an atomic orbital basis. I. Theory, J. Chem. Phys. 139 (2013). https://doi.org/10.1063/1.4824442.

[61] I. Lukačević, High pressure lattice dynamics, dielectric and thermodynamic properties of SrO, Phys. B Condens. Matter. 406 (2011) 3410–3416. https://doi.org/10.1016/j.physb.2011.06.010.

[62] S. Rondiya, Y. Jadhav, M. Nasane, S. Jadkar, N.Y. Dzade, Interface structure and band alignment of CZTS/CdS Heterojunction: An experimental and first-principles DFT investigation, Materials (Basel). 12 (2019). https://doi.org/10.3390/ma1224040.

[63] J.S. Shaikh, R.C. Pawar, R.S. Devan, Y.R. Ma, P.P. Salvi, S.S. Kolekar, P.S. Patil, Synthesis and characterization of Ru doped CuO thin films for supercapacitor based on Bronsted acidic ionic liquid, Electrochim. Acta. 56 (2011) 2127–2134. https://doi.org/10.1016/j.electacta.2010.11.046.

[64] S.S. Mali, B.M. Patil, C.A. Betty, P.N. Bhosale, Y.W. Oh, S.R. Jadkar, R.S. Devan, Y.R. Ma, P.S. Patil, Novel synthesis of kesterite Cu 2ZnSnS 4 nanoflakes by successive ionic layer adsorption and reaction technique: Characterization and application, Electrochim. Acta. 66 (2012) 216–221. https://doi.org/10.1016/j.electacta.2012.01.079.

[65] J.H. Lin, R.A. Patil, R.S. Devan, Z.A. Liu, Y.P. Wang, C.H. Ho, Y. Liou, Y.R. Ma, Photoluminescence mechanisms of metallic Zn nanospheres, semiconducting ZnO nanoballoons, and metal-semiconductor Zn/ZnO nanospheres, Sci. Rep. 4 (2014). https://doi.org/10.1038/srep06967.

[66] J.H. Lin, Y.J. Huang, Y.P. Su, C.A. Liu, R.S. Devan, C.H. Ho, Y.P. Wang, H.W. Lee, C.M. Chang, Y. Liou, Y.R. Ma, Room-temperature wide-range photoluminescence and

semiconducting characteristics of two-dimensional pure metallic Zn nanoplates, RSC Adv. 2 (2012) 2123–2127. https://doi.org/10.1039/c2ra00972b.

[67] S. Rondiya, A. Rokade, A. Jadhavar, S. Nair, M. Chaudhari, R. Kulkarni, A. Mayabadi, A. Funde, H. Pathan, S. Jadkar, Effect of calcination temperature on the properties of CZTS absorber layer prepared by RF sputtering for solar cell applications, Mater. Renew. Sustain. Energy. 6 (2017). https://doi.org/10.1007/s40243-017-0092-6.

[68] S.S. Mali, R.S. Devan, Y.R. Ma, C.A. Betty, P.N. Bhosale, R.P. Panmand, B.B. Kale, S.R. Jadkar, P.S. Patil, J.H. Kim, C.K. Hong, Effective light harvesting in CdS nanoparticle-sensitized rutile TiO 2 microspheres, Electrochim. Acta. 90 (2013) 666–672. https://doi.org/10.1016/j.electacta.2012.12.017.

[69] K. Diwate, A. Pawbake, S. Rondiya, R. Kulkarni, R. Waykar, A. Jadhavar, A. Rokade, A. Funde, K. Mohite, M. Shinde, H. Pathan, R. Devan, S. Jadkar, Substrate temperature dependent studies on properties of chemical spray pyrolysis deposited CdS thin films for solar cell applications, J. Semicond. 38 (2017). https://doi.org/10.1088/1674-4926/38/2/023001.

[70] B. John F. Moulder, William F. Stickle, Peter E. Sobol, Kenneth D, Handbook of XPS_sandeep.pdf, 2nd ed., Physical Electronics, 1992.

[71] R.S. Devan, V.P. Thakare, V. V. Antad, P.R. Chikate, R.T. Khare, M.A. More, R.S. Dhayal, S.I. Patil, Y.R. Ma, L. Schmidt-Mende, Nano-Heteroarchitectures of Two-Dimensional MoS2@ One-Dimensional Brookite TiO2 Nanorods: Prominent Electron Emitters for Displays, ACS Omega. 2 (2017) 2925–2934. https://doi.org/10.1021/acsomega.7b00345.

[72] J. Tao, J. Liu, J. He, K. Zhang, J. Jiang, L. Sun, P. Yang, J. Chu, Synthesis and characterization of Cu2ZnSnS4 thin films by the sulfurization of co-electrodeposited Cu-Zn-Sn-S precursor layers for solar cell applications, RSC Adv. 4 (2014) 23977–23984. https://doi.org/10.1039/c4ra02327g.

[73] J. Han, S.W. Shin, M.G. Gang, J.H. Kim, J.Y. Lee, Crystallization behaviour of co-sputtered Cu2ZnSnS4 precursor prepared by sequential sulfurization processes, Nanotechnology. 24 (2013) 95706. https://doi.org/10.1088/0957-4484/24/9/095706.

[74] K. Mokurala, S. Mallick, Effect of annealing atmosphere on quaternary chalcogenide-based counter electrodes in dye-sensitized solar cell performance: synthesis of Cu 2 FeSnS 4 and Cu 2 CdSnS 4 nanoparticles by thermal decomposition process, RSC Adv. 7 (2017) 15139–15148. https://doi.org/10.1039/C6RA28889H.

[75] X. Zhang, E. Fu, Y. Wang, C. Zhang, Fabrication of Cu 2 ZnSnS 4 (CZTS)

nanoparticle inks for growth of CZTS films for solar cells, Nanomaterials. 9 (2019) 336. https://doi.org/10.3390/nano9030336.

[76] J.H. Lee, H.J. Choi, W.M. Kim, J.H. Jeong, J.K. Park, Effect of pre-annealing on the phase formation and efficiency of CZTS solar cell prepared by sulfurization of Zn/(Cu,Sn) precursor with H2S gas, Sol. Energy. 136 (2016) 499–504. https://doi.org/10.1016/j.solener.2016.07.031.

[77] J.H. Lee, H.J. Choi, W.M. Kim, J.H. Jeong, J.K. Park, Effect of Post-annealing on the Solar Cell Performance of CuZnSnS4 Thin Film Prepared by Sulfurization of Stacked Metal Precursor with HS Gas, in: 2018 IEEE 7th World Conf. Photovolt. Energy Conversion, WCPEC 2018 - A Jt. Conf. 45th IEEE PVSC, 28th PVSEC 34th EU PVSEC, 2018: pp. 135–138. https://doi.org/10.1109/PVSC.2018.8547941.

[78] R.R. Thankalekshmi, A.C. Rastogi, Studies on process induced optoelectronic and structural modifications of CdS/CZTS heterojunction interface affecting solar cell efficiency, in: 2015 IEEE 42nd Photovolt. Spec. Conf. PVSC 2015, 2015: pp. 1–6. https://doi.org/10.1109/PVSC.2015.7355887.

[79] T. Wada, Y. Hashimoto, S. Nishiwaki, T. Satoh, S. Hayashi, T. Negami, H. Miyake, High-efficiency CIGS solar cells with modified CIGS surface, Sol. Energy Mater. Sol. Cells. 67 (2001) 305–310. https://doi.org/10.1016/S0927-0248(00)00296-8.

[80] B. Canava, O. Roussel, J.F. Guillemoles, D. Lincot, A. Etcheberry, Increasing solar cell efficiencies based on Cu(In,Ga)Se2 after a specific chemical and oxidant treatment, Phys. Status Solidi Curr. Top. Solid State Phys. 3 (2006) 2551–2554. https://doi.org/10.1002/pssc.200669614.

[81] A. Nadarajah, T. Smith, R. Könenkamp, Improved performance of nanowire-quantum-dot-polymer solar cells by chemical treatment of the quantum dot with ligand and solvent materials, Nanotechnology. 23 (2012) 485403. https://doi.org/10.1088/0957-4484/23/48/485403.

[82] S. Ji, T. Shi, X. Qiu, J. Zhang, G. Xu, C. Chen, Z. Jiang, C. Ye, A Route to phase Controllable Cu2ZnSn(S1-xSe x)4 nanocrystals with tunable energy bands, Sci. Rep. 3 (2013). https://doi.org/10.1038/srep02733.

[83] R. Dovesi, B. Kirtman, L. Maschio, J. Maul, F. Pascale, M. Rérat, Calculation of the Infrared Intensity of Crystalline Systems. A Comparison of Three Strategies Based on Berry Phase, Wannier Function, and Coupled-Perturbed Kohn-Sham Methods, J. Phys. Chem. C. 123 (2019) 8336–8346. https://doi.org/10.1021/acs.jpcc.8b08902.

Scheme 1. Facile hot-injection method setup for the synthesis of CZTS and CCTS NCs

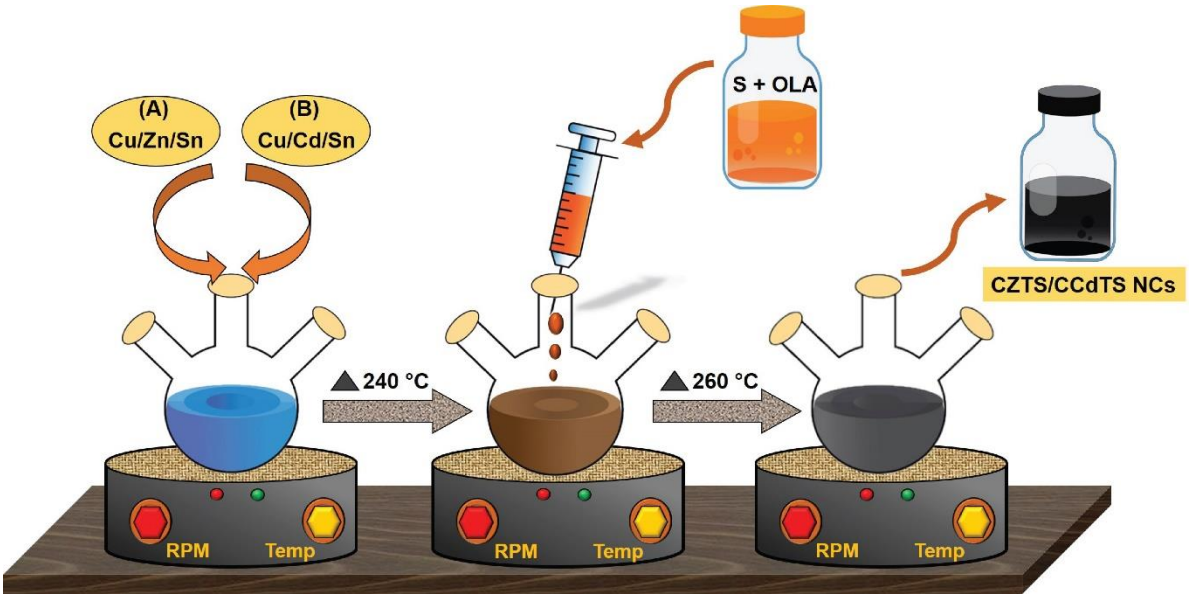

Fig. 1. (a) XRD pattern (b) Raman spectrum for the CZTS and CCTSNCs. Low-resolution TEM images (c, e) and HR-TEM images (d, f) recorded for CZTS and CCTS NCs, respectively.

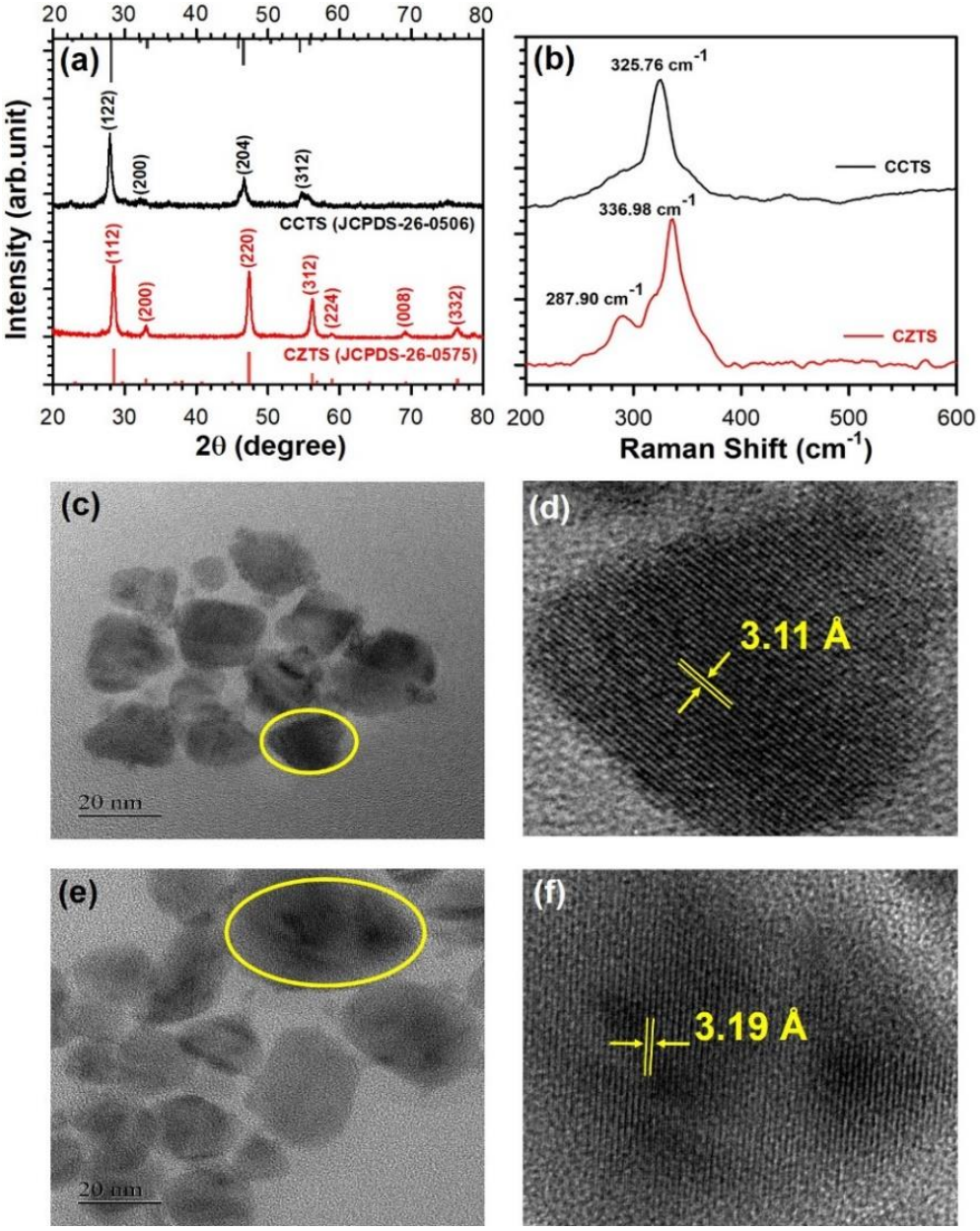

Fig. 2. Calculated Raman spectra of powder polycrystalline (a) CZTS and (b) CCTS. The reported spectra include temperature effects for the integrated intensities only and were re-normalized to the most prominent mode.

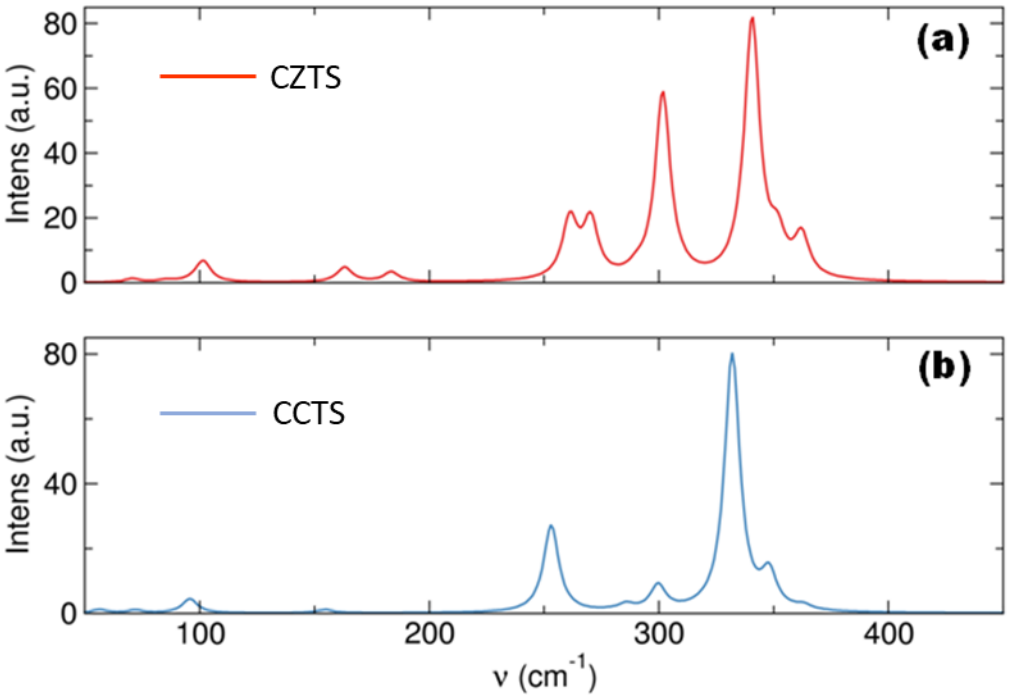

Fig. 3. Full phonon dispersion curves and the corresponding atom-projected partial phonon densities of state for CZTS and CCTS.

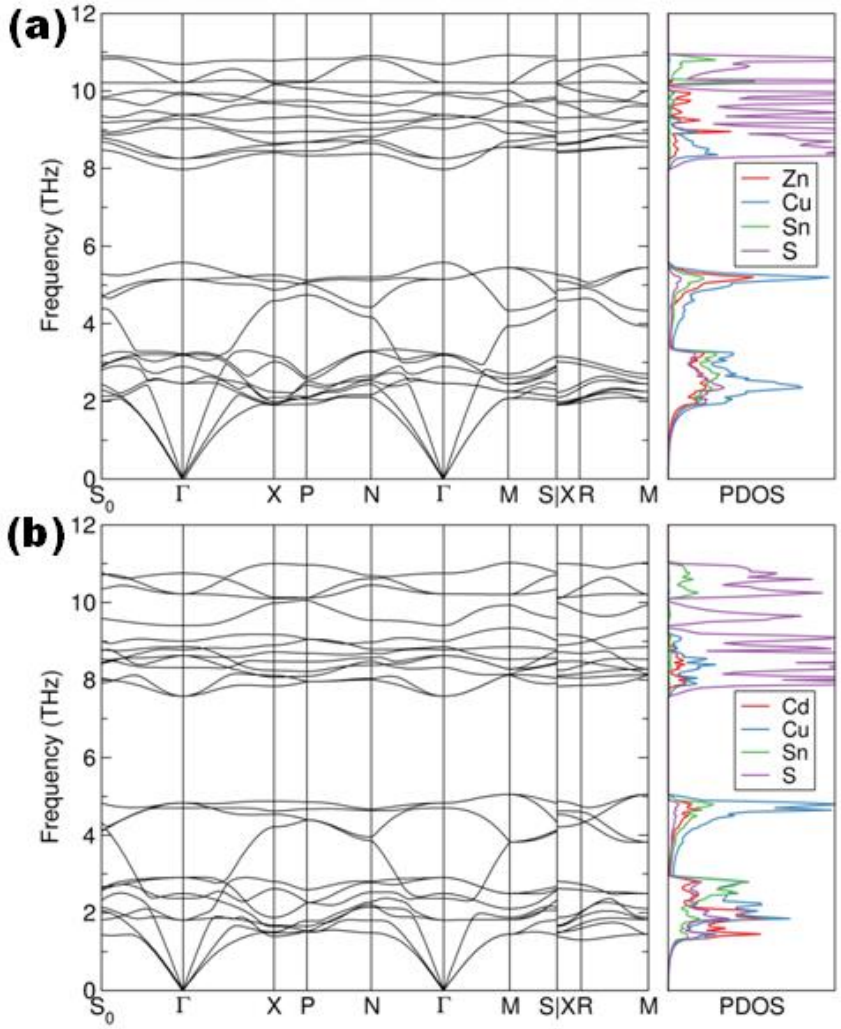

Fig. 4. High-resolution XPS spectra of (a) Cu(2p), (b) Zn(2p), (c) Sn(3d), and (d) S(2p) core levels of CZTS NCs, and (e) Cu(2p), (f) Cd(3d), (g) Sn(3d), and (h) S(2p) core levels of CCTS NCs. All the XPS spectra are deconvoluted with Voigt curve fitting function in the Shirley background.

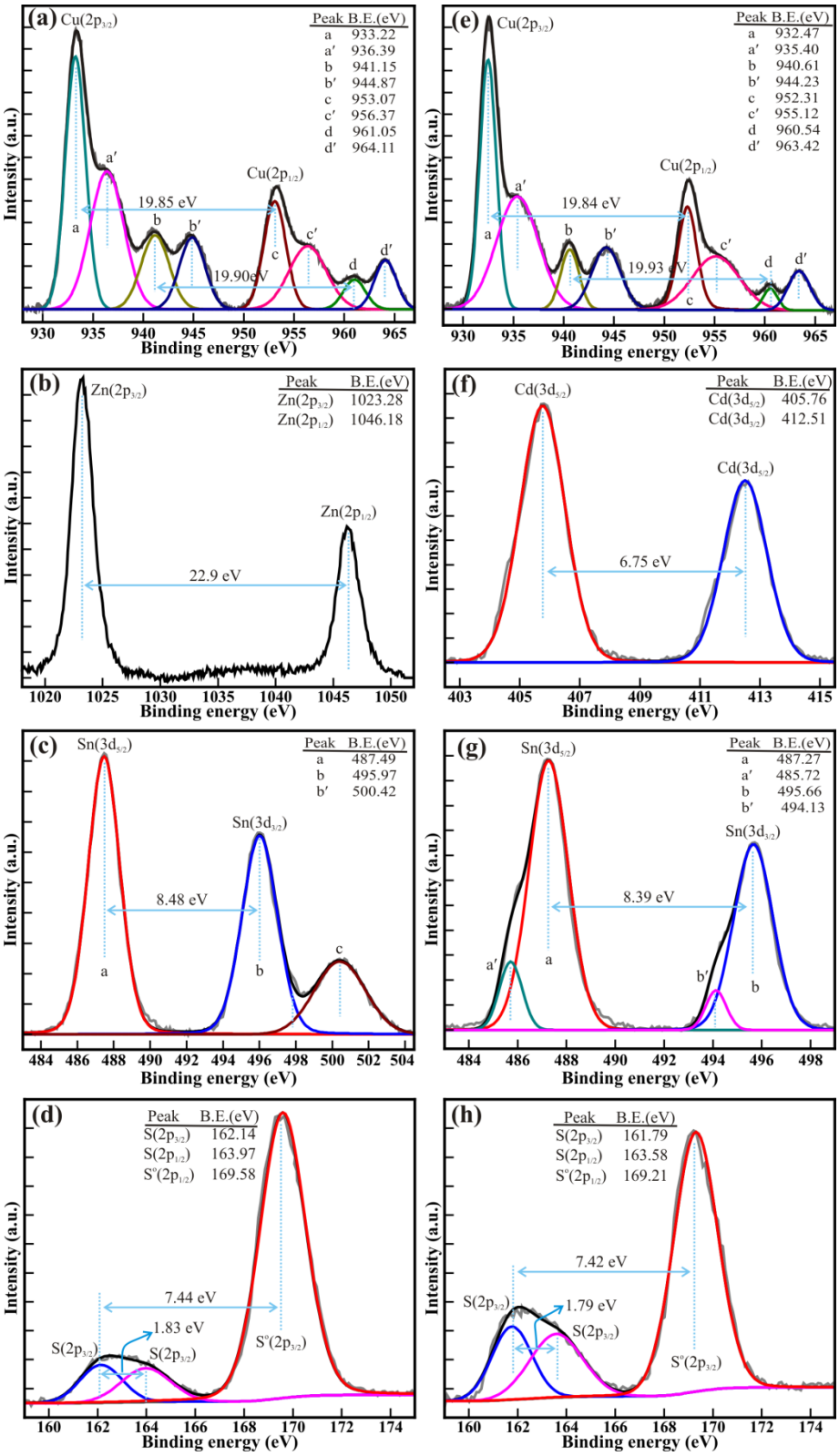

Fig. 5. (a) The UV−Vis-NIR absorbance spectra for CZTS and CCTS NCs with the inset showing the Tauc plot. (b) CZTS and CCTS NCs device architecture: FTO/TiO_2/CdS/CCTS/ZnS/S^{--}/S_n^-/ CuS/FTO. (c) Photovoltaic (J-V) characteristics of CZTS and CCTS NCs solar cells. (d) Schematic diagram for operating principle of a nanocrystal sensitized solar cell, solid arrows represent charge carrier transfer paths, whereas dotted lines indicate paths for detrimental back electron transfer.

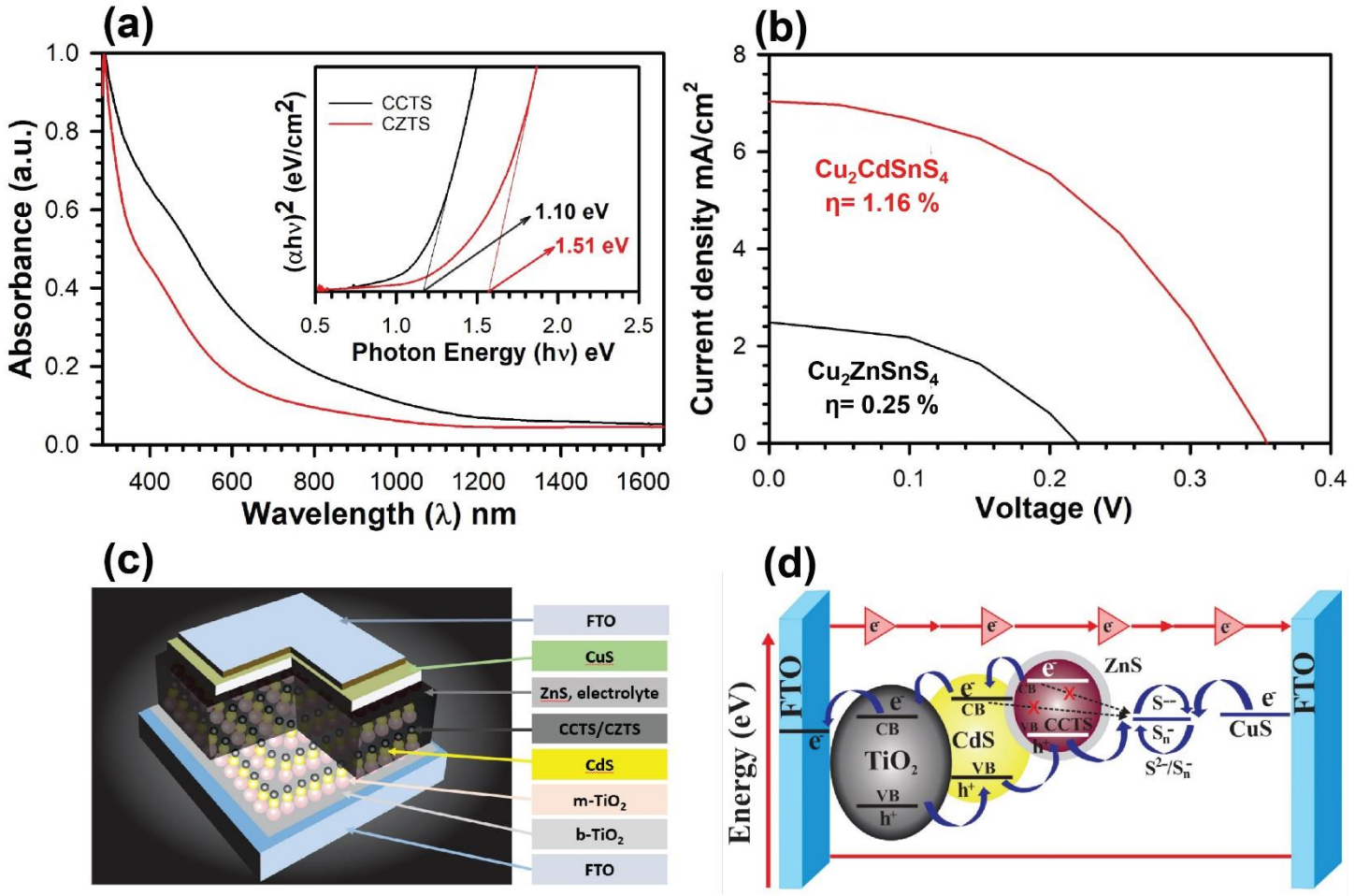

Table 1. Lattice parameters of CZTS and CCTS calculated using XRD pattern.

No.	Sample	D (nm)	d_{hkl} (Å)	Strain (ϵ_{hkl})	Dislocation density (ρ) (m^{-2})	Lattice parameter (Å)
1)	Cu_2ZnSnS_4	22.7	3.13	$6.70*10^{-3}$	$1.94*10^{15}$	a = b = 5.41, c = 10.88
2)	Cu_2CdSnS_4	19.4	3.19	$7.19*10^{-3}$	$2.65*10^{15}$	a = b = 5.53, c = 11.2

Table 2. Lattice parameters of CZTS and CCTS calculated using density functional theory (DFT).

		CZTS		CCTS	
		a (Å)	c (Å)	a (Å)	c (Å)
PBEsol		5.34	10.67	5.49	10.71
SC-B3LYP		5.45	10.88	5.61	10.88
Experiment	[83]	5.42	10.85	5.54	11.02
	[40]	5.43	10.87	5.45	10.76

Table 3. Calculated Raman properties of powder CZTS and CCTS. The temperature effect was taken for integrated intensities only and the integrated intensities were re-normalized so that the strongest mode is equal to 1000.

CZTS			CCTS		
Symmetry	ν (cm^{-1})	Intensity	Symmetry	ν (cm^{-1})	Intensity
E	70.69	14.30	E	56.25	13.72
B	85.54	8.73	B2	69.67	0.56
B	96.94	4.79	B1	71.99	10.86
E	101.53	82.85	E	95.71	55.56
E	163.14	57.59	B2	151.48	1.40
B	183.46	38.25	E	154.77	12.21
B	261.28	230.43	E	253.10	339.34
E	270.25	220.80	B2	278.99	2.53
A	290.23	25.97	E	285.84	24.00
A	301.70	724.37	A1	299.50	72.31
E	309.82	6.50	B1	300.10	25.54
B	335.15	21.96	A1	331.97	1000.00
A	340.65	1000.00	E	347.96	135.39
E	351.69	135.14	B2	363.11	16.34
B	362.17	157.95			

Table 4. Device performance, crystal structural parameters, and energy dispersive x-ray (EDS) analysis.

Material	Device Parameters	Device Performance	Composition Properties	Atomic Percentage (%)
Cu_2ZnSnS_4	Fill factor (FF)	0.44	Copper (Cu)	11.41
	Current density (J_{sc})	2.48 mA/cm^2	Zinc (Zn)	3.62
	Open circuit voltage (V_{oc})	0.22 V	Tin (Sn)	5.07
	PCE (η)	0.25 %	Sulfur (S)	19.30
Cu_2CdSnS_4	Fill factor (FF)	0.43	Copper (Cu)	14.89
	Current density (J_{sc})	7.50 mA/cm^2	Cadmium (Cd)	6.32
	Open circuit voltage (V_{oc})	0.35 V	Tin (Sn)	7.81
	PCE (η)	1.16 %	Sulfur (S)	29.07